Finite strain and rotation from fault-slip data

TRENTON T. CLADOUHOS and RICHARD W. ALLMENDINGER

Department of Geological Sciences, Cornell University, Ithaca, NY 14853-1504, U.S.A.

Abstract—The moment tensor summation (MTS) characterizes the infinitesimal strain of a region due to fault rupture during an earthquake. Tectonic strain on a much longer time scale can be found by applying the MTS to fault-slip data, which represent cumulative fault displacement. However, the traditional MTS assumes infinitesimal strain, which may not be appropriate for cumulative displacement on faults. Therefore, it is necessary to examine whether a finite strain treatment is more appropriate. We develop a method to find finite strain from fault-slip data (FSFS) and use it to illuminate two general faulting problems: finite strain and block rotation.

First, the FSFS method is compared to the MTS using both synthetic and real fault data. Strain due to faults must be high (> 60% elongation) before the infinitesimal strain approximation produces errors greater than the variation of typical field data. However, some regions do exhibit very high fault strains and require finite strain analysis.

Second, the FSFS method is used to solve for rotation in regions cut by domino-style faults, a common model for high fault strains and rotation. Given an arbitrary rigid boundary, the method can be used to relate fault strain and block rotation. For example, a paleomagnetic rotation of 40° requires fault strain with a minimum finite elongation of 41%.

INTRODUCTION

DISPLACEMENT along faults is the primary manifestation of upper crustal deformation in active orogenic belts. Therefore, fault-slip data must be analyzed to quantify strain magnitude and orientation. A planar fault can be characterized by three elements: the unit vector normal to the fault plane; the unit vector parallel to the direction of accumulated slip; and the scalar value of average fault displacement. The collection of these data in the field is often difficult, but allows one to characterize the strain magnitude and orientation of a region due to its population of faults. We use the term *fault strain* to describe the strain due to a population of faults within a region. Fault strain is unrelated to strain suffered by material within a shear zone. It may seem contradictory to represent fault displacement (inherently discontinuous deformation) as strain (an inherently continuous description). However the technique developed below and others like it (Molnar 1983, Jamison 1989) incorporate reasonable approximations to derive finite or infinitesimal strain magnitude and orientation from fault orientations and displacements.

By writing equations for extension and shortening along an arbitrary traverse across a fault, Freund (1970) was the first to quantify deformation due to the cumulative displacement of faults exposed at the surface. Reches (1976, 1978) introduced the continuum estimate and tensor notation to strain analysis of fault-slip data. The moment tensor summation (MTS) was developed to integrate the deformation due to earthquakes (Kostrov 1974, Molnar 1983). It has also been recast and used on fault-slip data. Marrett & Allmendinger (1990) introduced the use of the geometric moment (Sammis *et al.* 1987) to scale fault-slip tensors, and Jamison (1989) independently developed an infinitesimal fault strain

tensor. To apply either of these methods, both of which are analogous to Molnar's (1983) MTS, two general assumptions must be made. First, the faulted region, which is inherently discontinuous, must be approximated as a continuous medium in order to apply the principles of continuum mechanics. Second, infinitesimal strain theory must be adopted, which, although justifiable for seismicity, may not be appropriate for faults with large displacements relative to the size of the region.

In this paper, we investigate the second assumption by developing the *finite strain from fault-slip data* (FSFS) method, a tensor technique for determining the finite strain of a region due to faults within the region. In contrast with geometric methods which employ traverses (Freund 1970, Reches 1976, Wojtal 1989), this solution requires the dimensions of the faulted region to be known. This requirement may make the traverse methods more generally applicable; however when applicable, the FSFS method provides additional information and insight. In the first section of the paper, we develop the theoretical background for the FSFS method and illuminate the differences between the FSFS method and the MTS applied to fault-slip data. In the second section, the newly developed technique is tested on sample data sets and compared to results obtained from the MTS applied to fault-slip data. This comparison shows that total fault displacement must be as large as the diameter of the region before a significant difference (i.e. variations greater than those in typical field data) between the methods is noted. In the third section, equations are developed to relate the FSFS method to rotation of regions cut by 'domino-style' faults. This model is chosen because it is a well-known setting for extremely high fault strains that require finite strain analysis. Also, the model offers a mechanism to

explain rigid block rotation due to fault movement noted in many paleomagnetic studies.

THEORETICAL BACKGROUND

Finite homogeneous strain relates the initial and final states of a deformed body. The intermediate states are not addressed by this theory, so that progressive strain history need not be specified. Quantitative finite strain analysis of faults involves three steps: continuum estimation, multiplication and decomposition. We emphasize that this technique sacrifices geometric detail to attain a smoothed average of regional fault strain.

Continuum estimation

Faulting is an inherently discontinuous phenomenon. However, when the observational scale relative to the fault size is increased, the deformation may be approximated by continuous, homogeneous deformation (Reches 1976, 1978, Molnar 1983, Gauthier & Angelier 1985, Jamison 1989, Wojtal 1989). The motive for this step is clear—it allows application of continuum mechanics theory. Because strain is strictly a continuum measurement, calculating 'fault strain' (really an oxymoron) requires a continuum estimate of some sort. The continuum estimation made by analytical methods (Molnar 1983, Jamison 1989) involves estimating the shape of a circle cut and displaced by the fault as an ellipse (Figs. 1a–c). In spite of the necessity of such an estimation, its significance is seldom probed. When analyzing the kinematics of large fault strains, the estimate becomes more questionable because an offset circle begins to look less like an ellipse (Fig. 1c). However, one must bear in mind that the mechanics of the deformation are never approximated as continuous (Wojtal 1989). Simply the initial and final shape of the faulted regions are approximated as continuous.

Reches (1976), Gauthier & Angelier (1985) and Jamison (1989) quantify faulting by using the displacement gradient tensor referred to the undeformed state **D** (see Table 1 for list of mathematical symbols used throughout text). If $\hat{u}$ is the direction of accumulated slip, $\hat{n}$ is the fault normal (see Appendix for details), s the average displacement on the fault, and w the width of the faulted region (Fig. 1), then the components of the displacement gradient tensor are (Reches 1976, p. 127):

$$D_{ij} = \frac{s}{w}\,\hat{u}_i\hat{n}_j. \qquad (i,j = 1, 2, 3). \qquad (1)$$

In equation (1) and throughout the paper, north, east and down are $i = 1, 2$ and 3, respectively. The ratio s/w is the engineering shear strain, γ. This estimation is equivalent to distributing the fault displacement uniformly along the axis normal to the fault (Fig. 1c). The displacement gradient tensor defined by equation (1) differs only by a constant from the 'asymmetrical moment tensor' derived by Molnar (1983):
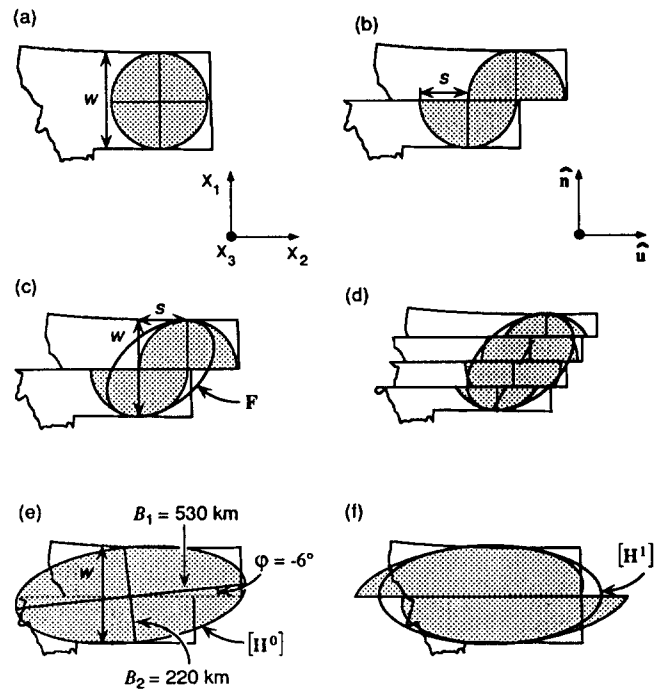
Fig. 1. (a) Two-dimensional slice perpendicular to fault plane and parallel to movement direction (movement plane) of generic unfaulted region (map of state of Montana) with width w. Circle is inscribed to track strain. Note co-ordinate system for Fig. 1. (b) Same view of Montana after right-lateral fault with fault normal, $\hat{n}$, unit slip direction, $\hat{u}$, and displacement, s. (c) Continuum estimation for circle in (b) superposed over true discontinuous final state. The deformation gradient tensor, **F**, relates the circle in (a) to the ellipse in (c). (d) Equivalent alternative to (c); three parallel faults with total shear equal to s. Dotted line is 'average' of broken vertical vectors. (e) Ellipse representing shape of deformed Montana shown in 1(b). Semi-axes, B_1 and B_2, and rotation angle, ϕ, are shown. To calculate a_{ij} from ϕ, we use $a_{11} = a_{22} = \cos(\phi)$, $a_{12} = -a_{21} = \sin(\phi)$, $a_{33} = 1$ and $a_{13} = a_{23} = a_{31} = a_{32} = 0$. [$H^0$] is found from equation (4). (f) Superposition of ellipse cut by fault of displacement $-s$ and continuum estimate of retrodeformed ellipse. [H^1], which is related to [H^0] by **F** (equation 15), should approximate undeformed shape of Montana.

$$M^*_{ij} = M_o \hat{u}_i \hat{n}_j, \qquad (2)$$

where M_o is the seismic moment, the product of the elastic shear modulus, average seismic slip and fault surface area. Whereas equation (1) is dimensionless, equation (2) must be divided by the volume of the region and the shear modulus in order to make the quantity dimensionless and calculate strain. Once this is done, the two formulations are identical for cylindrical and rectangular volumes and differ by a factor of 3/2 for spherical and ellipsoidal volumes.

Obviously, the choice of the width, w, over which to distribute the fault displacement is of paramount importance (see Jamison 1989). Analytically and graphically, shear strain and the width of a region are straightforward concepts; the ratio s/w is readily apparent in Fig. 1(c). The width simply represents the dimension of the region perpendicular to the fault plane. Using this fact we make a modification to account for two possibilities: (1) faulted regions will seldom be equant. Faults of different orientations will 'feel' different widths; and (2) although the width of the region perpendicular to a fault will not change, other dimensions will change as deformation progresses. Therefore, if the

Table 1. Symbols used in text. We use the standard convention that scalars and the components of vectors and tensors are italic, whereas the matrix notation of vectors and tensors are bold (i.e. D_{ij} vs $\mathbf{D}$)

Symbol	Equation	Parameter
$\mathbf{D}$, D_{ij}	(1)	material displacement gradient tensor referred to undeformed state
s	(1)	average displacement on fault
w	(1)	width of region perpendicular to fault
$\hat{\mathbf{u}}$, $\hat{u}_i$	(1)	unit vector in the direction of accumulated slip
$\hat{\mathbf{n}}$, $\hat{n}_i$	(1)	unit vector normal to the fault plane
γ	(1)	engineering shear strain, s/w
M^*_{ij}	(2)	asymmetric moment tensor (Molnar 1983)
M_o	(2)	seismic moment, μsA
$\mathbf{x}$	(3)	position vector in deformed state
B_i	(4)	principal semi-axes of ellipsoid representing shape of faulted region
a_{ij}	(4)	direction cosines of axes of ellipsoid representing faulted region
$[\mathbf{H}^n]$, $[H^n]_{ij}$	(4)	symmetric matrix that represents ellipsoid
t	(4)	the total number of faults in the faulted region
n	(4)	used as superscript to refer to a parameter of the nth fault
c_{ij}	(5)	transformation matrix from fault coordinates to geographic coordinates
$\mathbf{F}$	(8)	deformation gradient tensor referred to undeformed state
$\mathbf{F}^{-1}$	(8)	reciprocal deformation gradient tensor referred to undeformed state
$\mathbf{X}$	(8)	position vector in undeformed state
I, δ_{ij}	(9)	identity matrix, Kronecker delta
$[\mathbf{F}^{n*}]^{-1}$	(14)	the total reciprocal deformation gradient tensor up to the nth fault
$[\mathbf{F}^{t*}]^{-1}$	(14)	the total reciprocal deformation gradient tensor
$\mathbf{T}$	(16)	left stretch tensor
$\mathbf{S}$	(16)	right stretch tensor
$\mathbf{R}$	(16)	rotation tensor
v_{ij}	(17)	eigenvectors of left stretch tensor
V_{ij}	(17)	eigenvectors of right stretch tensor
ω	(21)	infinitesimal rotation tensor
ε	(21)	infinitesimal strain tensor
θ'_s, θ'_e	(23)	orientation of finite shortening and extension axes, Fig. 5(b)
ξ'	(24)	unit normal vector to rigid plane in deformed state
ξ	(24)	unit normal vector to rigid plane in undeformed state
$\mathbf{Q}$	(25)	external rotation necessary to completely describe fault deformation
Φ	(26)	rotation magnitude of fault blocks, $\Phi = a - a'$
Ω	(26)	rotation axis direction cosines
e_{ijk}	(26)	permutation symbol, $e_{123} = e_{312} = e_{231} = 1$
		$e_{321} = e_{213} = e_{132} = -1$
a	(31)	initial angle between fault and reference boundary
a'	(32)	final angle between fault and reference boundary

deformed region contains faults of various orientations, the width perpendicular to any fault may significantly change over the period of faulting. For these two reasons we estimate the deformed (geologically observable) shape of the region as an ellipsoid (Fig. 1e) and use the reciprocal deformation gradient tensor to retrodeform the region stepwise (Fig. 1f), at each step recalculating the width of the ellipsoid perpendicular to the fault.

We start by picking the ellipsoid that best approximates the shape of the deformed region (Fig. 1e). This ellipsoid will be defined by the lengths of the three orthonormal principle semi-axes, B_1, B_2 and B_3, and their respective directions, relative to standard geographic co-ordinates, expressed as unit vectors, a_{1j}, a_{2j} and a_{3j}. The equation for any quadratic form in $\mathbf{x}$ (including the equation for an ellipsoid) can be written as (Murdoch 1966, pp. 237–239):

$$\mathbf{x}^T \mathbf{H} \mathbf{x} = 1, \tag{3}$$

where $\mathbf{x}$ represents a vector variable and $\mathbf{H}$ a symmetric matrix. The components of $\mathbf{H}$ in geographic co-ordinates are (Malvern 1969, p. 32):

$$[H^0]_{ij} = a_{ip}a_{jp}\frac{1}{(B_p)^2} \qquad (i,j,p = 1,2,3). \tag{4}$$

We use the square brackets and superscript (i.e. ^{0}) to denote the ellipsoid calculated directly from the principal semi-axes, B_p. To generalize the procedure, below we introduce $[\mathbf{H}^n]$ ($[H^n]_{ij}$ in indicial form) to represent the ellipsoid retrodeformed by the first n faults. To find the width (w in Fig. 1e) of the ellipsoid represented by $[\mathbf{H}^n]$, we find the projection of the ellipsoid onto the plane containing $\hat{\mathbf{n}}$ and $\hat{\mathbf{u}}$. The transformation matrix $\mathbf{c}$, whose components are $c_{1j} = \hat{n}_j$, $c_{2j} = \hat{u}_j$ and $c_{3j} = (\hat{\mathbf{u}} \times \hat{\mathbf{n}})_j$, accomplishes the projection:

$$[H^n]'_{ij} = c_{ip}c_{jq}[H^n]_{pq} \qquad (i,j,p,q = 1,2,3). \tag{5}$$

The equation of the ellipse $[\mathbf{H}^n]'$ projected onto the $\hat{\mathbf{n}}$ $\hat{\mathbf{u}}$ plane becomes:

$$[H^n]'_{22}(x_2)^2 + 2[H^n]'_{12}(x_1 x_2) + [H^n]'_{11}(x_1)^2 = 1. \tag{6}$$

The width, w, represents the maximum dimension of the ellipse parallel to the x_1 axis (Fig. 1e). This can be found by setting the discriminant of equation (6) equal to zero and solving for x_1:

$$w^n = 2x_1^{max} = 2\sqrt{\frac{[H^n]'_{22}}{[H^n]'_{11}[H^n]'_{22} - [H^n]'^2_{12}}}. \quad (7)$$

Now the shear strain due to the nth fault is given by the ratio between the displacement on that fault s^n and the width of the region w^{n-1} prior to retrodeformation by that fault.

Multiplication

For infinitesimal strains the bulk displacement gradient tensor is simply the sum of the individual displacement gradients (D, equation 1) for each fault. For finite strain we introduce F, the deformation gradient tensor referred to the deformed state and its reciprocal, F^{-1}. F operates on a vector in the undeformed state X to give a vector in the deformed state x and F^{-1} operates in the reverse manner (Malvern 1969, p. 156):

$$x = F X \quad (8a)$$

and

$$X = F^{-1} x. \quad (8b)$$

We introduce both forms because F is more intuitive, representing deformation in the forward direction; however, we calculate F^{-1}, the deformation required to retrodeform a deformed region. For a single fault, F^{-1} will be calculated from the negative of the displacement. The relationship between D and F is by definition (Mase 1970, p. 80):

$$D \equiv F - I, \quad (9)$$

where I is the identity matrix. Combining equations (1) and (9) and adding a notation for the nth fault, the components of the reciprocal deformation gradient become:

$$[F^n]_{ij}^{-1} = \frac{-s^n}{w^n} \hat{u}_i^n \hat{n}_j^n + \delta_{ij}, \quad (10)$$

where δ_{ij} is the indicial form of the identity matrix. From equations (8) it can be seen that the imposition of successive large deformations is properly described by the product of individual deformation gradients tensors:

$$\chi = [F^2] X \quad (11a)$$

and

$$x = [F^1]\chi = [F^1][F^2] X, \quad (11b)$$

where χ has been deformed by $[F^2]$ but not $[F^1]$. For large displacements, multiplying deformation gradient tensors (F) is not equivalent to summing displacement gradient tensors (D). Reintroducing equation (9) we get:

$$[F^1][F^2] = ([D^1] + I)([D^2] + I)$$

$$= ([D^1] + [D^2] + [D^1][D^2] + I). \quad (12)$$

If we assume second- and higher-order terms (i.e. $[D^1][D^2]$, equation 12) to be zero, as is typical for infinitesimal strain analyses, then summation is equivalent to multiplication.

Equation (12) also highlights an unfortunate complication of finite strain theory. Matrix multiplication is not commutative and reversing the order of deformation yields

$$[F^2][F^1] = ([D^2] + [D^1] + [D^2][D^1] + I). \quad (13)$$

Equations (12) and (13) differ only in the second-order term. If $[D^1]$ and $[D^2]$ represent strain due to slip on parallel faults, $[D^1]$ and $[D^2]$ differ only be a scalar multiple and $[D^2][D^1]$ equals $[D^1][D^2]$. However, in general $[D^2][D^1]$ is not equal to $[D^1][D^2]$. Therefore, unless faults are parallel, we must be able to determine their relative ages from cross-cutting relations in order to correctly impose the strains.

Now we are prepared to combine the reciprocal deformation gradient tensors of multiple faults within the same region. The *total* reciprocal deformation gradient tensor $[F^{n*}]^{-1}$ due to n faults ordered from youngest to oldest (1 = youngest fault), can be calculated as

$$[F^{n*}]^{-1} = [F^n]^{-1} \cdots [F^2]^{-1}[F^1]^{-1}. \quad (14)$$

To complete the procedure, we find the shape of the region after retrodeforming by $[F^{n*}]^{-1}$. We write equation (3) in terms of the undeformed co-ordinates, X, instead of the deformed co-ordinates, x. Substituting equation (8a) into equation (3) gives:

$$[H^n] = [F^{n*}]^T[H^0][F^{n*}], \quad (15)$$

where $[H^n]$ represents the shape of the region (an ellipsoid) after retrodeforming up to the nth fault.

Now w^{n-1}, the width of the ellipsoid perpendicular to the nth fault prior to retrodeformation, can be used to calculate the deformation gradient tensor for each fault (equation 10). Thus we have developed an iterative process for quantifying fault deformation. By starting with equation (4) and then iterating equations (5), (7), (10), (14) and (15) from the youngest ($n = 1$) to the oldest ($n = t$) fault, we can find the bulk reciprocal deformation tensor, $[F'^*]^{-1}$, which can then be inverted to find the bulk deformation gradient tensor, $[F'^*]$. $[H']$ will correctly describe the shape of the undeformed region.

Multiple sets of simultaneous faults

The requirement of ordering faults from youngest to oldest for equation (14), presents practical problems for the finite strain method. In a three-dimensional strain field, multiple faults of various orientations may develop simultaneously (Reches 1978). Even in two-dimensional strain, coeval conjugate faults or faults with bends make it impossible to correctly choose fault order. The solution to this dilemma is suggested by the physical process—incremental slip. We can combine the deformation of two coeval faults by dividing the total slip on both faults into slip increments (s/a) and then iterating equations (5), (7), (10), (14) and (15) from 1 to a. In other words, instead of running the method on two faults with displacements s^1 and s^2, the method should be run for $2a$ faults with displacements s^1/a and s^2/a. If several
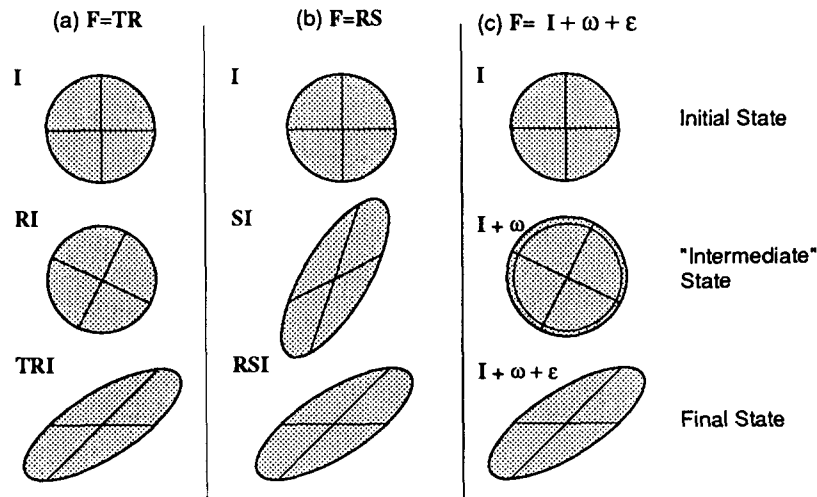
Fig. 2. Three alternative descriptions of the deformation gradient tensor, F. In each case the unit circle, represented by the identity matrix, I, is deformed. Initial and final states are identical; only 'intermediate' state differs. (a) Deformation described by rotation and then left stretch tensor. (b) Deformation described by right stretch tensor and then rotation. (c) Deformation described by infinitesimal rotation and strain tensors. Note 10% dilation of circle in 'intermediate' state.

faults are active at once, this expression can be generalized to many faults. The choice of slip increment (a) is arbitrary; the reciprocal deformation gradient tensor (equation 14) will always converge by 50 iterations and usually sooner. This modification should be used on coeval conjugate faults, and the difference will be significant in comparison with arbitrarily choosing an order of faulting. Major thrust faults, where different segments have different orientations, can be modeled by dividing the thrust into constant dip segments and assigning a displacement normalized by the length of the segment (see application below).

Decomposition

[F'^*] describes the total deformation due to the summed faults. It is useful to break deformation into pure strain and rigid body rotation components. The polar decomposition theorem states that any non-singular second-order tensor, F, is the product of an orthogonal rotation tensor, R, and a positive-definite symmetric tensor, S or T (Malvern 1969, pp. 172–181):

$$F = TR = RS. \tag{16}$$

In the first form of equation (16), the deformation consists of rotation R followed by stretch T, the left stretch tensor (Fig. 2a). The second form consists of stretch S, the right stretch tensor, followed by rotation R (Fig. 2b). These representations do not imply that the deformed state was achieved by one of two possible combinations of pure rotation and pure shear. Rather S may be considered to act in the undeformed state on the position vector X while T acts in the deformed state on x. The stretch tensors are calculated from (Malvern 1969, p. 174):

$$T = \sqrt{FF^T} \tag{17a}$$

and

$$S = \sqrt{F^T F}. \tag{17b}$$

The eigenvectors (v_{ij} and V_{ij}, respectively) of the tensors T and S give the orientations of the orthogonal set of principal stretch axes; the eigenvalues (T_i, S_i) are the principal stretch magnitudes. Principal finite elongations, e_i, are given by $S_i - 1$ or $T_i - 1$.

The rotation tensor, R, rotates the principal axes of S into the principal axes of T and its components are calculated from the eigenvalues of the stretch axes (Malvern 1969, p. 177):

$$R_{ij} = v_{ki}V_{kj} \qquad (i, j, k = 1, 2, 3). \tag{18}$$

The left stretch tensor, T, which describes the strain of a deformed region in the deformed co-ordinate system, is preferred for analyzing the strain that a deformed body has suffered. Because S describes strain in the undeformed co-ordinate system which the geologist never sees, S is not generally useful to geoscientists (Owens 1973).

Molnar (1983), Gauthier & Angelier (1985) and Jamison (1989) assume that the deformation due to faulting is infinitesimal, and they decompose the displacement gradient into symmetric and antisymmetric parts, ε and ω, respectively. Written in indical form this becomes:

$$D_{ij} = \omega_{ij} + \varepsilon_{ij}, \tag{19}$$

where

$$\omega_{ij} = \tfrac{1}{2}(D_{ij} - D_{ji}) \tag{20a}$$

and

$$\varepsilon_{ij} = \tfrac{1}{2}(D_{ij} + D_{ji}) \tag{20b}.$$

Such a mathematical operation can always be performed. At large strains, however, ω and ε do not represent pure rotation and pure strain, respectively. For example, in Fig. 2(c), $\omega_{32} = -\omega_{23} = 0.5$. This represents 0.5 radians (28.6°) of rotation and 10% dila-
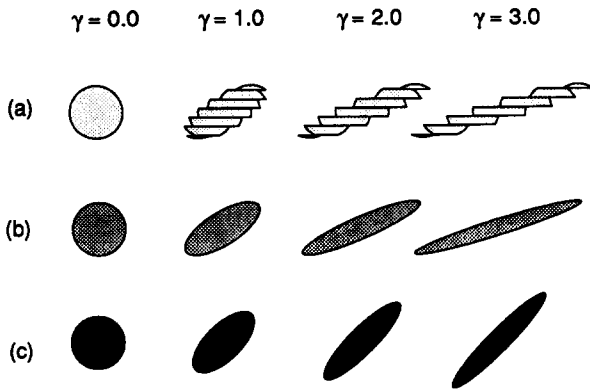
Fig. 3. Graphical comparison between (a) faulted region, (b) finite strain estimate (left stretch tensor, T) and (c) infinitesimal strain estimate (infinitesimal strain tensor, ε) for three different shear strains.

tion (intermediate circle). The finite rotation (R) gives $\tan^{-1}(0.5) = 22.6°$ rotation and no strain.

STRAIN MAGNITUDE AND ORIENTATION

Given the fault variables $\hat{n}$, $\hat{u}$ and s, and the shape of the region, $[H^0]$, we can calculate the maximum stretch magnitude and orientation (the eigenvalues and eigenvectors, respectively, of the left stretch tensor, $T = \sqrt{[F'^*][F'^*]^T}$) of a faulted region. For the simple case of a single fault or a single set of parallel faults, we can solve for strain magnitude and orientation in terms of one independent variable, γ, the shear strain. This is shown graphically in Fig. 3 and solved analytically below.

Magnitude

Ramsay & Huber (1983, p. 30) give the solution for maximum finite stretch magnitude, T_1, as a function of the shear strain ($\gamma = s/w$) assuming constant volume:

$$T_1 = \sqrt{1 + \frac{\gamma^2}{2} + \frac{\gamma}{2}\sqrt{\gamma^2 + 4}}. \tag{21}$$

The more familiar maximum infinitesimal stretch magnitude, $E_1 + 1$, is the first-degree Taylor polynomial for equation (21) when $\gamma = 0$. Then stretch becomes linear with respect to shear strain:

$$T_1 \approx E_1 + 1 = 1 + \frac{\gamma}{2}. \tag{22}$$

In Fig. 4, equations (21) and (22) are graphed for comparison. For $\gamma = 1$, finite strain theory gives $T_1 = 1.62$ whereas infinitesimal theory gives $E_1 + 1 = 1.5$. Thus at a finite elongation of 62%, infinitesimal theory would estimate only 50% elongation.

Orientation

For a single fault the infinitesimal (or incremental) strain axes are oriented 45° to the fault plane. Seismological P and T axes are incremental strain axes (Marrett &
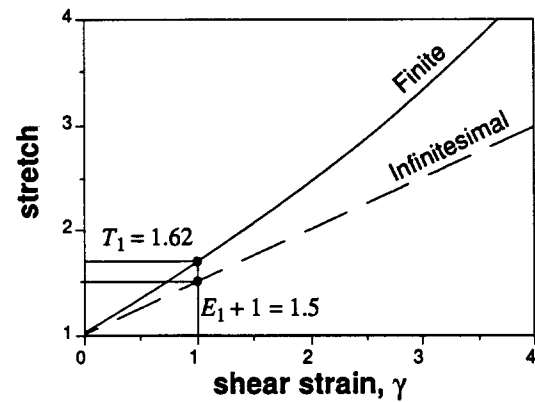

Fig. 4. Comparison of finite (equation 21) and infinitesimal (equation 22) stretch magnitudes.

Allmendinger 1990). On the other hand, finite strain axes rotate as displacement, s, increases. If stretch axis orientation is defined as shown in Fig. 5b, the angles are given by (Ramsay & Huber 1983, p. 27):

$$\theta'_s = 90° + \frac{1}{2}\tan^{-1}\left(-\frac{2}{\gamma}\right) \tag{23a}$$

and

$$\theta'_e = 180° + \frac{1}{2}\tan^{-1}\left(-\frac{2}{\gamma}\right), \tag{23b}$$

where θ'_s is the acute angle between the axis of shortening and the fault plane and θ'_e is the obtuse angle between the axis of extension and the fault plane.

At a shear strain of 1 (equivalent to a finite elongation of 62%), the finite axis will differ from the infinitesimal axes by 13° (Fig. 5a). A 13° error due to assuming infinitesimal strain is comparable to orientation variation of normal field data. Field data can vary due to two factors; measurement error, and fault plane and striae undulation. The first type of error is typically small; a geologist should be able to measure plane orientations and line directions accurate within a few degrees. In our experience, the second type of 'error' can be much larger. It is common for an individual fault measurement (strike, dip, striae azimuth or striae plunge) to vary about the average value by $\pm5°$. Thus, although the total uncertainty depends on several factors (displacement, diameter, fault orientation, and striae direction), finite strain methods should always be used when the total shear strain is above unity ($\gamma > 1$).

APPLICATIONS: STRAIN MAGNITUDE AND ORIENTATION

Synthetic data from Wojtal (1989)

Traverse methods (Freund 1970, Reches 1976, Wojtal 1989) involve measuring fault displacement and orientations on arbitrary traverses across the faulted region. From this data, finite strain magnitude and orientation can be derived. Wojtal (1989) illustrated his method on the synthetic data set shown in Fig. 6.
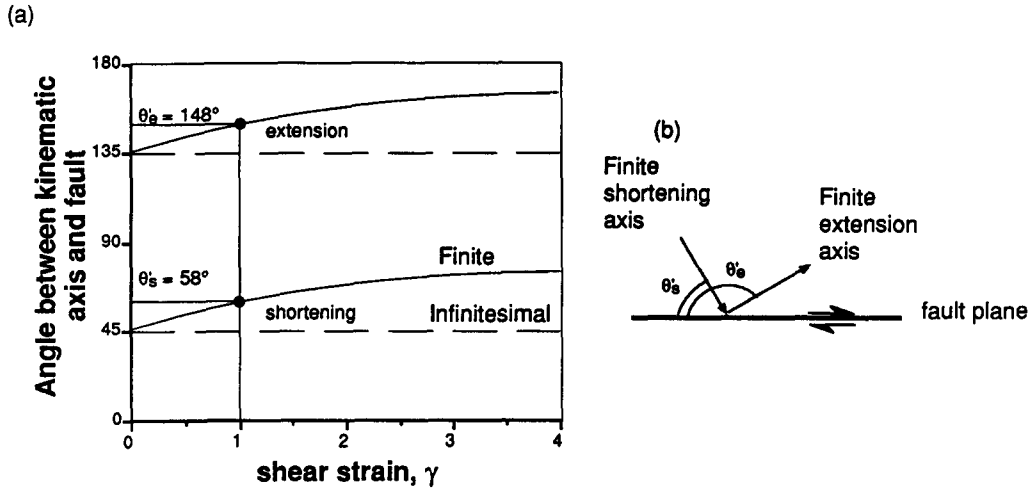
(a)

Fig. 5. (a) Comparison of the orientation of finite (equation 23) and infinitesimal stretch axes. (b) Co-ordinate system.

The objective of the FSFS method and Wojtal's (1989) method are identical; only the procedures are different. Therefore, a comparison of both analyses of Fig. 6 offers a check for the FSFS method. In this synthetic model, two generations of evenly spaced faults cut the region. It is straightforward to measure the displacements (numbers in Figs. 6b & c) on each of these faults. We start our analysis by estimating the ellipsoid, [$\mathbf{H}^0$] (equation 4) that best fits the shape of the region in Fig. 6(c). The third semi-axes (perpendicular to the page) can be arbitrarily chosen as unity in this two-dimensional

example. Equation (7) calculates the width (w^0) of the ellipse and then [$\mathbf{F}^1$]$^{-1}$ (equation 10) can be calculated for the youngest generation of parallel faults. Iteration of equations (7), (10) and (14) gives [$\mathbf{F}^{2*}$]$^{-1}$ which can be inverted and then decomposed to find the stretch, $\mathbf{T}$ (equation 17a). The eigenvalues of $\mathbf{T}$, which represent the principal stretch magnitudes are $T_1 = 2.04$, $T_2 = 1$, and $T_3 = 0.49$. The stretch axis orientations are found from the eigenvectors v_{ij}. Thus we have characterized the finite strain ellipse (Fig. 6d) for the region shown in Fig. 6(c). The fault displacements (shear strains)

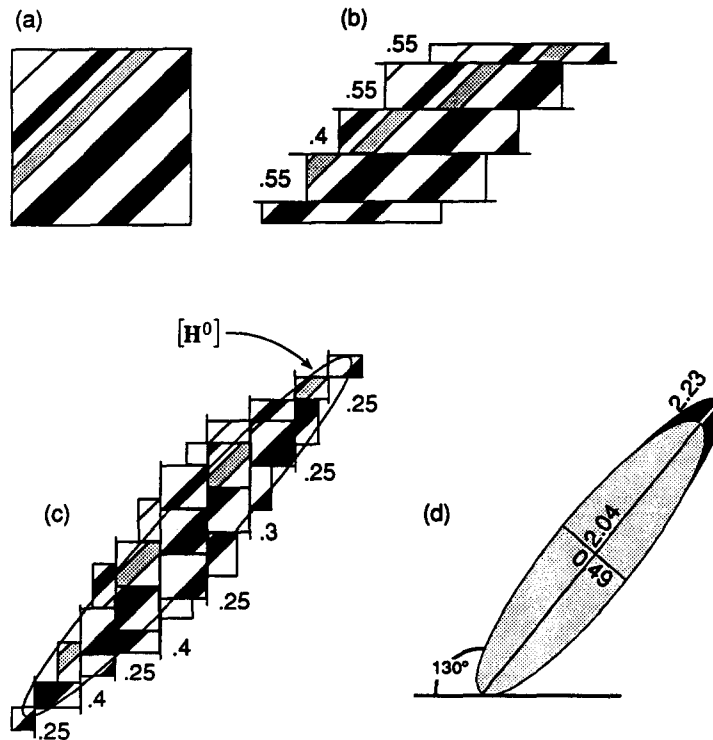Fig. 6. Analysis of synthetic data from Wojtal (1989). (a) Undeformed region. (b) Region cut by one fault set. Numbers are displacements in arbitrary units. (c) Region cut by two fault sets. Superposed ellipse is estimate of the shape of the region, [$\mathbf{H}^0$]. (d) Gray ellipse is the finite strain calculated by the FSFS method. Black ellipse is the finite strain estimated by Wojtal (1989).
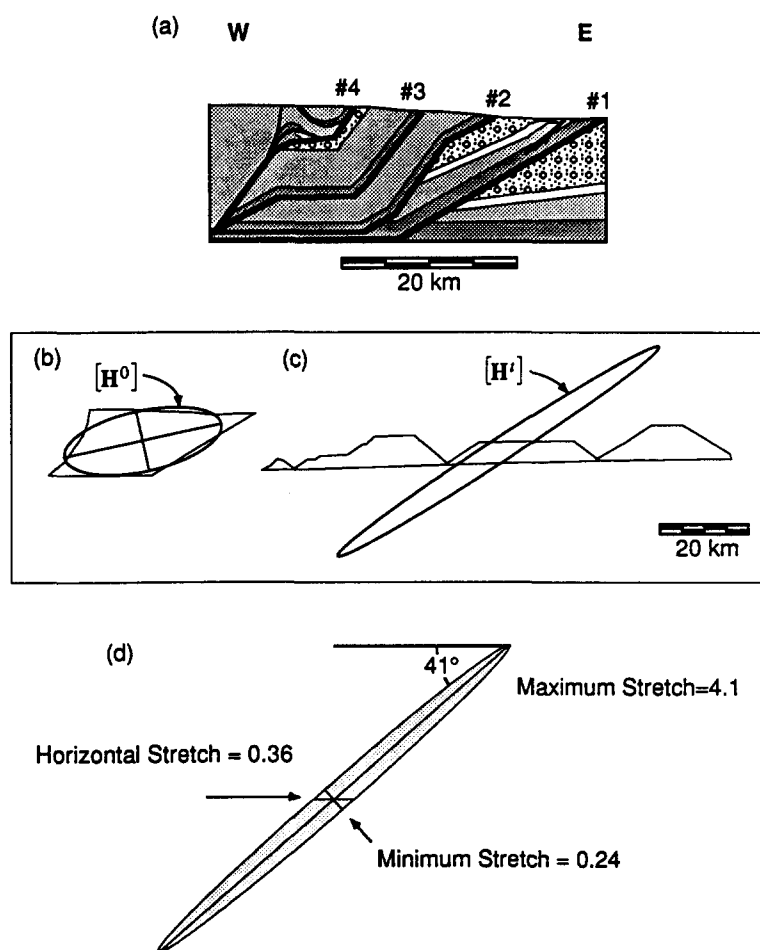
Fig. 7. Example from the Precordillera thrust belt. (a) Balanced cross-section of Allmendinger *et al.* (1990). See Table 2 for fault displacements. (b) Estimated ellipse [$\mathbf{H}^0$] superposed over shape of faulted region. Major semi-axis is 18 km and plunges 12° to the west. Minor semi-axis is 6.6 km. Scale for (b) and (c) is 50% of (a). (c) Undeformed ellipse [$\mathbf{H}^i$] superposed over palinspastic restoration of Allmendinger *et al.* (1990). Major semi-axis is 44 km and plunges 34° to the west. Minor semi-axis is 2.7 km. The discrepancy in orientation between the undeformed ellipse and the palinspastic restoration is explained in the 'Fault Strain and Rotation' section. (d) Strain of upper plate of Precordillera fold and thrust belt as determined by the FSFS method.

imposed in Figs. 6(b) & (c) correspond to a homogenous strain with stretches of $T_1 = 2.05$ and $T_3 = 0.48$; Wojtal's (1989) graphical method gave $T_1 = 2.23$ and $T_3 = 0.44$.

Precordillera fold and thrust belt

To apply the FSFS method to a field example, we briefly examine the fault strain in the Precordillera of Argentina, a thin-skinned fold and thrust belt. Allmendinger *et al.* (1990) present a balanced cross-section of the thrust belt (Fig. 7a) from which we derive fault displacements and dips. The thrust belt has four major thrusts, each of which have kinks. We treat each non-planar thrust as a series of simultaneous faults with different dips (Table 2). Segment displacements are normalized by segment lengths. The ellipsoid [$\mathbf{H}^0$] is shown superimposed on the outline of the deformed area in Fig. 7(b).

Employing the FSFS method with the simultaneous fault amendment we find that the maximum shortening is 76% (1.0–0.24) and dips 49° toward the foreland (Fig. 7d). Allmendinger *et al.* (1990) calculated about 70% horizontal shortening from the cross-section; the FSFS method yields 64% horizontal shortening. These are

high strain values, and the finite strain method is clearly preferred.

Horizontal shortening across the Precordillera is abnormally high; shortening in most foreland thrust belts is

Table 2. Input data for FSFS analysis of Precordillera fold and thrust belt. Thrusts are ordered from youngest to oldest (Fig. 7a). Each thrust was divided into constant dip segments and segment displacements were normalized by segment lengths

Thrust	Total s (km)	Segment dip (°)	Normalized s (km)
1	27	30	27.0
2	20	30	6.0
		55	10.0
		30	4.0
3	29	55	11.2
		0	9.4
		30	8.4
4	21	55	4.5
		0	4.7
		30	3.1
		55	8.7

nearer to 50%. However, even at this more typical strain ($T_1 > 2$, $\gamma > 1.5$), the infinitesimal method significantly underestimates strain magnitude and misidentifies strain orientation (cf. Figs. 4 and 5). Although this example demonstrates the application of the FSFS method to thrust belts, we emphasize that it is not necessarily desirable to do so. Most of the interesting geometric detail is lost in applying the continuum assumption.

Notice the shape and orientation of the undeformed region is shown in Fig. 7(c). The aspect ratio of the undeformed ellipsoid is nearly identical to that derived by Allmendinger et al.'s (1990) palinspastic restoration shown in the background of Fig. 7(c). However, the ellipse is rotated counterclockwise 33°. This disparity is due to the fact that [$\mathbf{F}'^*$] does not completely describe the deformation. Also notice the average 30°W dip of the strata in the balanced cross-section (Fig. 7a). These two issues are related because the basal detachment forces a counterclockwise rotation of the strata. We will solve the problem of fault strain and rotation in the next section.
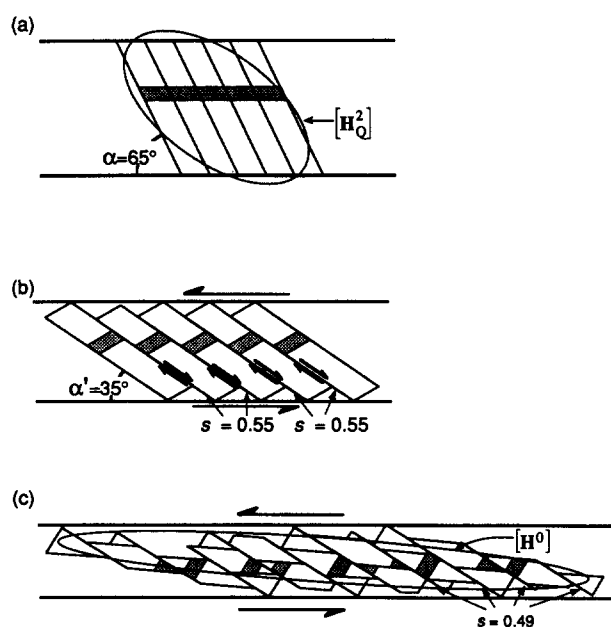

Fig. 8. Domino blocks model. (a) Initial configuration, bold lines are rigid reference boundary. (b) Region deformed by one fault set. Fault displacements (s) are shown in arbitrary units. (c) Region deformed by two fault sets. Ellipse [$\mathbf{H}^0$] in (c) was chosen to represent deformed area. Ellipse [$\mathbf{H}_Q^2$] in (a) was calculated from equation (30).

FAULT-STRAIN AND ROTATION

Block rotation is an important consequence of fault deformation yet to be addressed. Although faulting does not *always* create rotations, rotation of faults and fault blocks is quite common. Paleomagnetic studies in regions cut by strike-slip faults often show vertical-axis rotations (e.g. Ron et al. 1984, 1990). As mentioned above, the thrust sheets in the Precordillera example have experienced an average horizontal axis rotation of 30°.

Unfortunately, decomposing deformation into pure strain (S or T) and pure rotation (R) does not give block rotations. The tensor **R** describes the rotation of the material lines in the initial state that end up parallel to the principal stretch axes in the final state. To show that this rotation is *not* related to rigid block rotation as measured by paleomagnetic sampling, a distinction must be made between the continuum estimation and the actual discontinuous fault blocks. Notice that in Figs. 1(b) & (d), neither the faults nor blocks have rotated. When the faulted region is viewed as a continuous package, an apparent rotation of material lines is recognized (dotted line in Fig. 1d). However, the actual segments of the broken vectors do not rotate (thin line segments in Fig. 1d). Thus, **R** does not describe the rotation that would be measured by paleomagnetic studies within a rigid block in a faulted region. In fact, non-rotating strike-slip faults cannot create coherent large-scale vertical-axis block rotation like those often identified by paleomagnetic rotations.

Jackson & McKenzie (1988) also argue against using the rotation tensor derived from the asymmetric moment tensor summation (Molnar 1983) to determine paleomagnetic rotations. Their argument hinges on the inability of seismic observations to differentiate between

the rotation of the boundaries of a region and rotation of the faults. Below we argue that the MTS or FSFS method alone can *never* be used to determine rigid block rotation. In addition to the fault-strain information determined by the MTS of FSFS method, the orientation of a rigid reference boundary is needed to find block rotation (Garfunkel & Ron 1985).

Thompson (1960) developed a simple model to relate simultaneous tilting and normal faulting in the Basin and Range Province. To explain vertical axis rotations by strike-slip faults, Freund (1974) adopted a similar model. The domino-style fault blocks model, as it has become known, has been widely applied to extensional regimes (Proffett 1977, Miller et al. 1983, Mandl 1987) as well as to high strain strike-slip regimes (Ron et al. 1984, 1990). The FSFS method can be used on data that conform to this model, once the implications of the domino-style fault blocks model are further understood.

The model's key feature is that a rigid non-rotating boundary (bold lines in Fig. 8) forces the faults and fault blocks to rotate because the blocks cannot be displaced past this boundary (Garfunkel & Ron 1985). The rigid reference boundary is usually assumed to be a detachment or master fault that separates faulted and unfaulted regions.

Now the task is to relate shear magnitude and direction (fault orientation and displacement) in domino-style terrains to block rotation. Garfunkel & Ron (1985) attack this problem from the opposite direction by deriving fault strain from paleomagnetic rotation. In order to use the FSFS method to solve for block rotation, we must derive rotation from fault displacement.

We start by specifying the orientation of the rigid boundary (a plane) using the unit vector normal to the
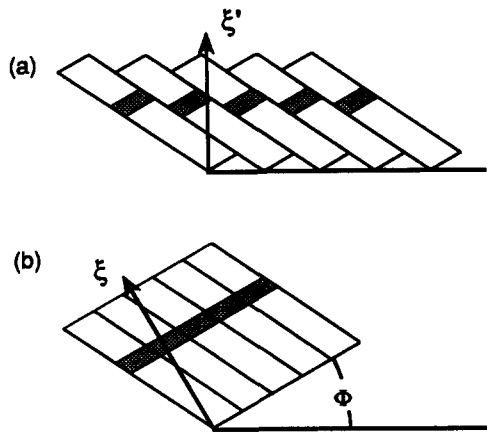
Fig. 9. Domino blocks model. (a) Deformed region, ξ' is unit normal to rigid plane. (b) Undeformed region, assuming no rotation of faults, ξ is calculated from equation (24). Φ gives the external rotation forced by the rigid reference boundary.

plane in the deformed state, ξ' (Fig. 9). The normal to the plane in the undeformed state, ξ, is (March 1932, p. 294, Lipshie 1984, p. 315):

$$\xi = [\mathbf{F}'^*]^T \xi'. \tag{24}$$

However, ξ is calculated assuming no external rotation (Fig. 9b). We seek an orthogonal rotation tensor, $\mathbf{Q}$, that when combined with $[\mathbf{F}'^*]$ ensures that the rigid plane (ξ') is not rotated by the deformation. That is, find $\mathbf{Q}$ such that,

$$\lambda\, \xi' = [\mathbf{F}'^*\mathbf{Q}]^T \xi'. \tag{25}$$

The constant λ is necessary in equation (25) because although ξ' can not rotate, it will strain. It must be made clear that $\mathbf{Q}$, the external rotation, is unrelated to $\mathbf{R}$ (equation 16), the continuum rotation. In the complete finite strain description of the deformation, an undeformed vector will first be rotated by $\mathbf{Q}$, then rotated by $\mathbf{R}$, and then stretched by $\mathbf{T}$.

For two square tensors $\mathbf{A}$ and $\mathbf{B}$, $[\mathbf{AB}]^T = \mathbf{B}^T\mathbf{A}^T$ and for an orthogonal tensor $\mathbf{Q}$, $\mathbf{Q}^T = \mathbf{Q}^{-1}$ (Malvern 1969, pp. 37 and 383). These properties and equation (24) allow us to rewrite equation (25) as,

$$\lambda\, \xi' = \mathbf{Q}^{-1}\xi. \tag{26}$$

Thus $\mathbf{Q}^{-1}$ rotates ξ to $\lambda\xi'$, and $\mathbf{Q}$ rotates $\lambda\xi'$ to ξ. The components of $\mathbf{Q}$ are given by the unit vector representing the axis of the rotation Ω and the magnitude of the rotation, Φ (LePichon $et\ al.$ 1973, p. 37):

$$Q_{ij} = \Omega_i\Omega_j(1 - \cos\Phi) - e_{ijk}\Omega_k \sin\Phi + \delta_{ij}\cos\Phi, \tag{27}$$

where e_{ijk} is the permutation symbol (Malvern 1969, p. 21). Because the rotation axis, Ω (a unit vector), will be perpendicular to both ξ' and ξ, it can be found from their cross product:

$$\Omega = \frac{\xi \times \xi'}{|\xi \times \xi'|}. \tag{28}$$

Furthermore the angle between ξ' and ξ is the magnitude of rotation Φ which can be found from the dot product:

$$\Phi = \cos^{-1}\left(\xi \cdot \left(\frac{\xi'}{|\xi'|}\right)\right). \tag{29}$$

Now we can return to the problem discussed at the end of the Precordillera fold and thrust belt example. If the basal detachment (strike $= 0°$, dip $= 1°\text{W}$) is chosen as the rigid plane, we find that $\Phi = 33°$. Furthermore the correct shape and orientation of the undeformed region can be found from

$$[\mathbf{H}_Q^t] = [\mathbf{F}'^*\mathbf{Q}]^T[\mathbf{H}^0]\,[\mathbf{F}'^*\mathbf{Q}]. \tag{30}$$

Applying equation (30) we find coincidence of the undeformed ellipse and the palinspastic reconstruction of Allmendinger $et\ al.$ (1990).

In order to write equations and make graphs that will explicitly represent rotation as a function of fault strain and geometry, we start with only one fault set (Fig. 8b). Garfunkel & Ron (1985) solve for rotation, Φ, as a function of shear strain, γ, and the initial angle between the fault and the reference boundary, α:

$$\cot(\Phi) = \frac{1}{\gamma\sin^2(\alpha)} + \cot(\alpha). \tag{31}$$

They use the convention that $\Phi > 0$ is a counterclockwise rotation and $\gamma > 0$ is a right lateral fault. To find Φ as a function of α', the final angle between the fault and the reference boundary, substitute $\alpha' = \alpha + \Phi$ into equation (31) and rearrange to find:
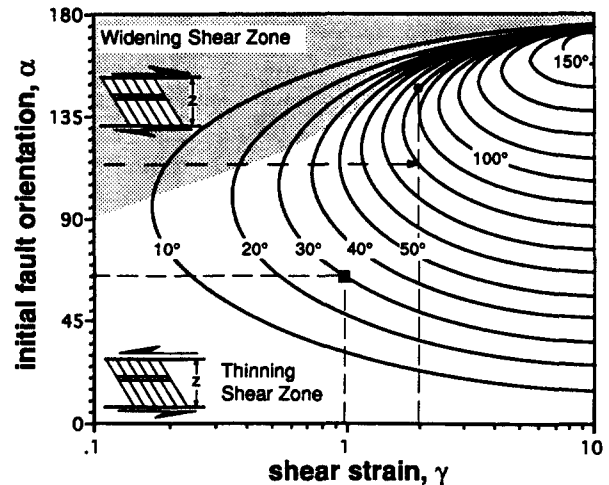

Fig. 10. Graph derived from equation (31) showing the relation between fault rotation (contours), initial fault orientation (vertical axis), and shear strain (horizontal axis). If two of the three parameters are known, then the third can be found using this graph. For example, the filled square shows position of the single-generation domino-block model in Fig. 8(b) ($\alpha = 65°$ and $\Phi = 30°$, therefore $\gamma \approx 1$). In the shaded region, the dimension across the region perpendicular to the rigid boundary (z) increases with increasing shear strain. In the unshaded region the dimension decreases, more typical of domino blocks models. For example, the arrow shows the rotation path as shear strain increased in the Transverse Ranges of southern California. First the faulted region widened and later thinned. To use final fault orientation (equation 32) instead of initial fault orientation, invert the left-hand axis ($0°$ at the top and $180°$ at the bottom). The filled circle denotes the parameters in the Transverse Ranges. The rotation ($\Phi = 80°$) and final orientation between domino faults and the rigid boundary ($\alpha' = 30°$) are known; the shear strain of two, read from this figure, is used to derive displacements for faults in the Transverse Range (Table 3).
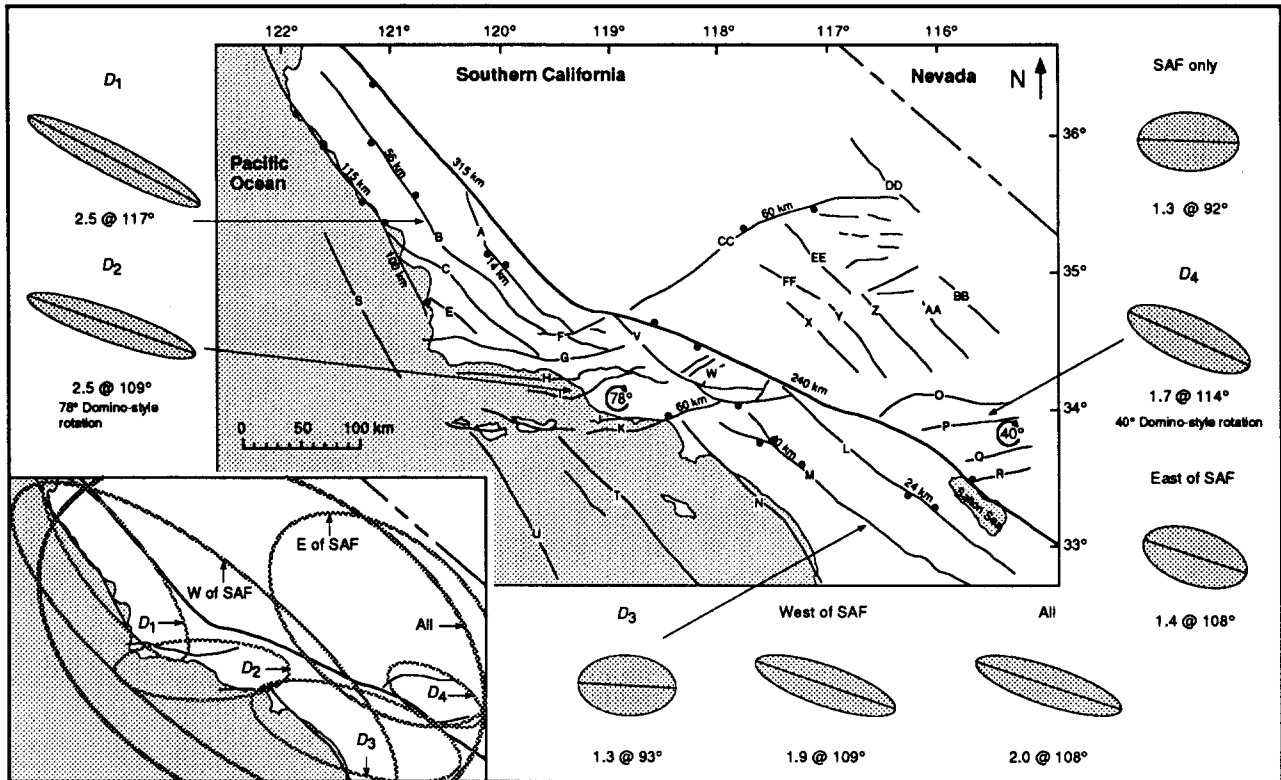
Fig. 11. San Andreas Fault and adjacent areas. Map from Hornafius *et al.* (1986). Letters referring to faults are keyed to Table 3. Fault displacements are indicated by piercing points (filled circles). Paleomagnetic rotations are shown as circular arrows with magnitude inside. Shown in the inset at the lower left are the elliptical strain domains [H^0] defined in this paper (Table 3). Strain ellipses around perimeter are for each of the domains. The maximum principal strain magnitude and orientation are given below each ellipse.

$$\cot(\Phi) = \frac{1}{\gamma \sin^2(\alpha')} - \cot(\alpha'). \qquad (32)$$

Thus, for a single set of shear planes, we can determine the rotation of a region (Φ) given the shear strain (γ) and the final or initial fault orientation (Fig. 10). Notice the importance of the orientation of the rigid boundary. If the rigid boundary is parallel to the faults ($\alpha = 0°$), there will be no rotation. If the initial or final orientation of the rigid boundary is perpendicular to the faults ($\alpha = 90°$), the block rotation will be $\tan^{-1} \gamma$. Clearly the 'non-rotating' faults discussed in the previous section are simply a specific case ($\alpha = 0°$) of this more general model.

Starting at a given initial fault orientation, a horizontal path from left to right on Fig. 10 indicates rotation as shear strain progresses. If the path is within the shaded region the shear zone widens (z increases, Fig. 10); in the unshaded region the shear zone thins (z decreases, Fig. 10). Figure 10 can also be used to estimate the minimum shear on one fault set necessary to create a paleomagnetic rotation. If, for example, a paleomagnetic rotation of 40° is thought to result from slip on one set of parallel rotating faults, the 'nose' of the 40° contour indicates a minimum shear strain of 0.7 to produce this rotation. This corresponds to a finite elongation of 41% (equation 21). Figure 10 provides a rapid way to assess whether local faulting produces sufficient strain to cause a measured paleomagnetic rotation.

Note that while regional shear of the domino blocks is

left-lateral, the sense of each rotating fault is right-lateral. Twiss *et al.* (1991) explain this potential kinematic discrepancy by applying the continuum theory of micropolar kinematics. In their scheme, two independent scales of rotation, microrotation (rotation of the blocks) and macrorotation (rotation of the region) are defined. The justification for two scales of rotation is that fault zones are composed of granular material. Although the method of Twiss *et al.* (1991) can be successfully used to interpret and predict slickenline patterns, it does not address strain or total rotation due to faulting.

Domino-style fault blocks example

As a test of the quantitative domino block model presented above, we find strain magnitude, orientation and rotation for the model shown in Fig. 8(c). With the displacement data shown in Figs. 8(b) & (c) and the ellipse [H^0] shown in Fig. 8(c), we can find the strain and rotation for the region due to the 14 faults. The FSFS analysis of the model in Fig. 8(c) gives a maximum stretch of 2.7 oriented nearly parallel to the rigid boundary and a minimum stretch of 0.37 nearly perpendicular to the rigid boundary. If the unit normal to the rigid plane, ξ', is chosen and equations (24), (28) and (29) used, the FSFS analysis gives the block rotation due to the faults within the region as 60°; as can be verified by measurement on Fig. 8(c).

Real-world examples of the domino-style fault block

Table 3. Input for FSFS analysis of southern California. The parameters used for each fault: σ and δ are the strike and dip of the fault plane, respectively, α and β are the striae azimuth and plunge, respectively, and s is the displacement. Displacements were estimated in four ways: H = displacement explicitly given by Hornafius *et al.* (1986), R = displacement implied by reconstructions of Hornafius *et al.* (1986), P = displacement constrained by paleomagnetic rotations given by Hornafius *et al.* (1986) and L = displacement estimated from trace length. The domain names are also shown in Fig. 10. The semi-axes lengths (B_1 and B_2) and orientation (ϕ) for each domain's ellipse are given. To calculate a_{ij} from ϕ, we use $a_{11} = a_{22} = \cos(\phi)$, $a_{12} = -a_{21} = \sin(\phi)$, $a_{33} = 1$ and $a_{13} = a_{23} = a_{31} = a_{32} = 0$

Fault		σ, δ (°)	α, β (°)	Sense	s (km)	Source of s	Domain
A	San Juan Chimineas	140 90	140 0	RL	14	H	D_1
B	Rinconada	140 90	140 0	RL	56	H	$B_1 = 50$ km
C	Los Osos	130 90	130 0	RL	35	R	$B_2 = 170$ km
D	Hosgri	140 90	140 0	RL	110	H	$\phi = 53°$
E	Orcutt	129 90	129 0	RL	10	R	
F	Big Pine	75 90	75 0	LL	14	H	D_2
G	Santa Ynez	90 90	90 0	LL	32	P	
H	San Cayento	90 90	90 0	LL	32	P	$B_1 = 45$ km
I	Oak Ridge	84 90	84 0	LL	32	P	$B_2 = 133$ km
J	Malibu Coast	84 90	84 0	LL	60	R	$\phi = 0°$
K	Dume	90 90	90 0	LL	20	R	
L	San Jacinto	130 90	130 0	RL	24	H	D_3
M	Elsinore	130 90	130 0	RL	40	H	$B_1 = 60$ km
N	Newport	135 90	135 0	RL	20	R	$B_2 = 165$ km $\phi = 18°$
O	Pinto Mountain	85 90	85 0	LL	26	P	D_4
P	Blue Cut	84 90	84 0	LL	26	P	$B_1 = 35$
Q	Chiriaco	80 90	80 0	LL	26	P	$B_2 = 78$
R	Salton Creek	80 90	80 0	LL	26	P	$\phi = 29°$
S	Santa Lucia	150 90	150 0	RL	20	L	Other west of SAF
T	San Clemente	138 90	138 0	RL	20	L	
U	Santa Rosa	152 90	152 0	LL	20	L	$B_1 = 120$ km
V	San Gabriel	120 90	120 0	RL	60	L	$B_2 = 360$ km
W	Unnamed	62 90	62 0	LL	5	L	$\phi = 33°$
W	Unnamed	60 90	60 0	LL	5	L	
W	Unnamed	54 90	54 0	LL	5	L	
X	Helendale	136 90	136 0	RL	20	L	Other east of SAF
Y	Lenwood	144 90	144 0	RL	20	L	
Z	Calico	140 90	140 0	RL	20	L	$B_1 = 125$ km
AA	Ludlow	140 90	140 0	RL	20	L	$B_2 = 200$ km
BB	Bristol Mountain	135 90	135 0	RL	20	L	$\phi = 40°$
CC	Garlock	68 90	68 0	LL	60	H	
DD	Death Valley	137 90	137 0	RL	30	L	
EE	Blackwater	137 90	137 0	RL	30	L	
FF	Lockhart	120 90	120 0	RL	20	L	
SAF		130 90	130 0	RL	300	H	$B_1 = 240$ km
							$B_2 = 360$ km $\phi = 29°$

model are numerous. Ron *et al.* (1990) summarized a field study in the Mount Herman area adjacent to the left-lateral Dead Sea transform fault. The study included two parts: (1) paleomagnetic sampling that indicated 69° ± 13° vertical axis rotation; and (2) fault measurements that indicate one active and two inactive sets of minor faults. Without addressing the displacement magnitudes on the faults, Ron *et al.* (1990), conclude that the faults represent three generations of domino-style faults that are responsible for the paleomagnetic rotation. Using the orientations of the three fault sets, the orientation of the Dead Sea Transform (the rigid boundary) and the shape of the faulted region (Ron *et al.* 1990), we can estimate that shear strains slightly greater than 1 on each fault set are necessary to account for the measured paleomagnetic rotation (see the Appendix). Also, this analysis gives the maximum (horizontal) stretch for the deformed region as 2.6 perpendicular to the rigid boundary.

San Andreas Fault and adjacent areas

As a final example, we apply the FSFS method to southern California adjacent to the San Andreas Fault. Although the primary feature of the region is the San Andreas, numerous smaller faults record the regional fault strain of this diffuse plate boundary. To find fault orientations, displacements and paleomagnetic rotations we used the data compiled by Hornafius *et al.* (1986) (Fig. 11 and Table 3). To apply the FSFS method, we define four separate strain domains. Elliptical domains were chosen such that the faults cut the boundaries of the ellipse (Fig. 11, inset); the semi-axes lengths and orientations of the domain ellipses are given in Table 3. The fault displacements in D_1 and D_3 were taken directly from Hornafius *et al.* (1986) (Table 3). In D_2 and D_4, we used the paleomagnetic rotation and Fig. 10 to estimate γ. For example, to produce 80° of rotation in the Transverse Ranges (D_2) a shear strain of approxi-

mately 2 is needed (Fig. 10). The width perpendicular to the faults of the D_2 ellipse is about 90 km, therefore, total left-slip fault displacement should be near 180 km. In both D_2 and D_4, the San Andreas was used as the rigid reference boundary. We assume that in all domains the faults within moved simultaneously, therefore we used the simultaneous fault modification with an increment (a) of 10.

Figure 11 summarizes the finite strain analysis as gray ellipses. Notice that, although D_2 rotated and D_1 did not, the two domains have similar strain magnitudes and orientations. Further south on both sides of the San Andreas in D_3 and D_4, the strains seem to be much lower. The ellipse labeled 'SAF only' is the strain of the region enclosed by the large ellipse due to only the San Andreas Fault. The large ellipse is meant to include the entire active plate boundary as evidenced by the faulting shown in Fig. 11. Three ellipses represent 'composite' strains found by combining domains. Although applying the FSFS method in this way is less rigorous than as applied to coherent structural domains, the results are helpful for summarizing regional strain.

The calculated maximum principal shortening direction due to all of the faults is oriented about 70° to the strike of the San Andreas Fault. The axes of folds in the vicinity of the San Andreas Fault are virtually parallel to the fault (Mount & Suppe 1987). The existence of two sets of strain features, faults and folds, with different strain orientations is a further indication of decoupling of the relative plate motion. One component is low-drag strike-slip displacement on the San Andreas and adjacent faults; the other is related to compression perpendicular to the San Andreas (Mount & Suppe 1987).

CONCLUSIONS

We have developed a technique for determining the finite strain of a region due to faults within the region based on the same concepts as the moment tensor summation. Finite strain magnitude, orientation and block rotation can all be calculated with this method. The FSFS method was applied to two synthetic and three real world examples to demonstrate its utility. All the examples were two-dimensional due to the available data sets; however, the method is not limited to two-dimensional analysis.

Because fault displacement is inherently discontinuous and strain is an inherently continuous concept, it may seem contradictory to represent fault displacement as strain. However, the FSFS method provides a shorthand to describe the change of shape and block rotation of a region due to faults within that region. For most faulted areas, the traditional MTS applied to fault-slip data (Jamison 1989, Marrett & Allmendinger 1990) will correctly calculate the strain but not block rotations. The FSFS method developed here should be used in fold and thrust belts, high strain regions adjacent to major structures and to solve for block rotations due to faulting.

REFERENCES

Allmendinger, R. W., Figueroa, D., Snyder, D., Beer, J., Mpodozis, C. & Isacks, B. L. 1990. Foreland shortening and crustal balancing in the Andes at 30°S latitude. *Tectonics* 9, 789–809.

Freund, R. 1970. The geometry of the faulting in the Galilee. *Israel J. Earth Sci.* 19, 117–140.

Freund, R. 1972. Remarks on the paper "The geometry of the faulting in the Galilee" (Freund, 1970). *Israel J. Earth Sci.* 21, 61–66.

Freund, R. 1974. Kinematics of transform and transcurrent faults. *Tectonophysics* 21, 93–134.

Garfunkel, Z. & Ron, H. 1985. Block rotation and deformation by strike-slip faults: 2. The properties of a type of macroscopic discontinuous deformation. *J. geophys. Res.* 90, 8589–8602.

Gauthier, B. & Angelier, A. 1985. Fault tectonics and deformation: a method of quantification using field data. *Earth Planet Sci. Lett.* 74, 137–148.

Hornafius, J. S., Luyendyk, B. P., Terres, R. R. & Kamerling, M. J. 1986. Timing and extent of Neogene tectonic rotation in the western Transverse Ranges, California. *Bull geol. Soc. Am.* 97, 1476–1487.

Jackson, J. & McKenzie, D. 1988. The relationship between plate motions and seismic moment tensors, and the rates of active deformation in the Mediterranean and Middle East. *Geophys. J.* 93, 45–73.

Jamison, W. R. 1989. Fault-fracture strain in Wingate Sandstone. *J. Struct. Geol.* 11, 959–974.

Kostrov, B. V. 1974. Seismic moment and energy of earthquakes, and seismic flow of rock. *Izv. Acad. Sci. USSR Phys. Solid Earth* 1, 23–44.

LePichon, X., Francheteau, J. & Bonnin, J. 1973. *Plate Tectonics*. Elsevier, Amsterdam.

Lipshie, S. R. 1984. Development of phyllosilicate preferred orientation in naturally and experimentally metamorphosed and deformed rocks. Unpublished Ph.D dissertation, University of California, Los Angeles, California.

Malvern, L. E. 1969. *Introduction to the Mechanics of a Continuous Medium*. Prentice-Hall, Englewood Cliffs, New Jersey.

Mandl, G. 1987. Tectonic deformation by rotating parallel faults: the bookshelf mechanism. *Tectonophysics* 141, 277–316.

March, A. 1932. Mathematische theorie der regelung nach der korngestalt bei affiner deformation. *Z. Kristallogr.* 81, 285–297.

Marrett, R. & Allmendinger, R. W. 1990. Kinematic analysis of fault-slip data. *J. Struct. Geol.* 12, 973–986.

Mase, G. E. 1970. *Schaum's Outline of Theory and Problems of Continuum Mechanics*. McGraw-Hill, New York.

Miller, E. L., Gans, P. B. & Garing, J. 1983. The Snake Range décollement: an exhumed mid-Tertiary ductile–brittle transition. *Tectonics* 2, 239–263.

Molnar, P. 1983. Average regional strain due to slip on numerous faults of different orientations. *J. geophys. Res.* 88, 6430–6432.

Mount, V. S. & Suppe, J. 1987. State of stress near the San Andreas fault: Implications for wrench tectonics. *Geology* 15, 1143–1146.

Murdoch, D. C. 1966. *Analytic Geometry with an Introduction to Vectors and Matrices*. John Wiley & Sons, New York.

Nur, A., Ron, H. & Scotti, O. 1986. Fault mechanics and the kinematics of block rotations. *Geology* 14, 746–749.

Nye, J. F. 1985. *Physical Properties of Crystals; Their Representation by Tensors and Matrices* (2nd edn). Oxford University Press, Oxford.

Owens, W. H. 1973. Strain modification of angular density distributions. *Tectonophysics* 16, 249–261.

Proffett, J. M., Jr. 1977. Cenozoic geology of the Yerrington district, Nevada, and implications for the nature and origin of Basin and Range faulting. *Bull. geol. Soc. Am.* 88, 247–266.

Ramsay, J. G. & Huber, M. I. 1983. *The Techniques of Modern Structural Geology*. Academic Press, London.

Reches, Z. 1976. Analysis of joints in two monoclines in Israel. *Bull geol. Soc. Am.* 87, 1654–1662.

Reches, Z. 1978. Analysis of faulting in three dimensional strain field. *Tectonophysics* 47, 109–129.

Ron, H., Freund, R., Garfunkel, Z. & Nur, A. 1984. Block rotations by strike-slip faulting: structural and paleomagnetic evidence. *J. geophys. Res.* **89**, 6256–6270.

Ron, H., Nur, A. & Eyal, Y. 1990. Multiple strike-slip fault sets: a case study from the Dead Sea transform. *Tectonics* **9**, 1421–1431.

Sammis, C., King, G. C. P. & Biegel, R. 1987. Kinematics of gouge formation. *Pure & Appl. Geophys.* **125**, 777–812.

Thompson, G. A. 1960. Problem of Late Cenozoic structure of the basin ranges. *Int. Geol. Congr. Rep.* **XVIII**, 62–66.

Twiss, R. J., Protzman, G. M. & Hurst, S. D. 1991. Theory of slickenline patterns based on the velocity gradient tensor and microrotation. *Tectonophysics* **186**, 215–239.

Wojtal, S. 1983. Finite deformation in thrust sheets and their material properties. Unpublished Ph.D. thesis, Johns Hopkins University, Baltimore, Maryland.

Wojtal, S. 1989. Measuring displacement gradients and strains in faulted rocks. *J. Struct. Geol.* **11**, 669–678.

APPENDIX

Representation of fault-slip datum as two vectors

Let an orthonormal basis be defined by north ($\hat{e}_1$), east ($\hat{e}_2$) and down ($\hat{e}_3$). The relation between measured fault data and the unit vectors representing the fault normal and the direction of accumulated slip is given by:

$$\hat{n} = - \sin(\delta)\sin(\sigma)\hat{e}_1 + \sin(\delta)\cos(\sigma)\hat{e}_2 - \cos(\delta)\hat{e}_3 \quad (A1)$$

$$\hat{u} = \cos(\alpha)\cos(\beta)\hat{e}_1 + \sin(\alpha)\cos(\beta)\hat{e}_2 + \sin(\beta)\hat{e}_3 \quad (A2)$$

and

$$\hat{b} = \hat{n} \times \hat{u}, \quad (A3)$$

where σ and δ are the strike and dip of the fault plane (right-hand rule), respectively, and α and β are the trend and plunge of the fault striae.

FSFS analysis of fault-slip and rotation data from Ron et al. (1990)

This analysis is necessarily approximate; nonetheless, it demonstrates an interesting application of the FSFS method. The map in fig. 2(a) of Ron *et al.* (1990) shows a study area of elliptical shape. The major semi-axis (B_1) is 12.3 km, the trend is 60° and plunge, 0°. The minor semi-axis (B_3) is 7.7 km, the trend is 150° and plunge, 0°. We chose a vertical intermediate semi-axis (B_2) with a length of 5 km. The strike of the Dead Sea Transform in the area varies from 0° to 30°; we chose a rigid plane with strike and dip of 20° and 90°, respectively. Table 1 of Ron *et al.* (1990) summarizes the fault data; the average orientation of fault planes in the youngest, intermediate and oldest fault sets are 331° 85°S, 295° 83°S, and 254° 89°N, respectively.

For simplicity we assigned the same total displacement to each fault set and ran the FSFS method using the above data. Total displacement of 23 km on each set produced a total counterclockwise rotation of 69°. This displacement corresponds to shear strains slightly greater than 1 on each fault set.